Numerical Analysis of Rocket Plume Impingement During Reusable Launcher Landing and Development of an Optimized Correlation for Wall Heat Flux Prediction

Angelo Romano *, Fabio Pisano, Daniele Cardillo, Francesco Battista

Posted Date: 19 March 2026

doi: 10.20944/preprints202603.1386.v1

Keywords: plume impingement; shock-wall interaction; reusable launcher landing; *LOx/CH4* engine; wall heat flux prediction; particle swarm optimization

 doi:10.20944/preprints202603.1386.v1

Article

Numerical Analysis of Rocket Plume Impingement During Reusable Launcher Landing and Development of an Optimized Correlation for Wall Heat Flux Prediction

Angelo Romano [1,*], Fabio Pisano [2], Daniele Cardillo [1] and Francesco Battista [1]

[1] Italian Aerospace Research Center, Space Propulsion Unit
[2] Industrial Engineering Department, University of Naples "Federico II"
* Correspondence: a.romano@cira.it; Tel.: +39-0823-62-3785

Abstract

During the powered landing phase of reusable launch vehicles, the interaction between the rocket exhaust plume and the landing surface generates intense and highly non uniform thermal loads. Reliable prediction of wall heat flux is therefore essential for the design of landing pads and thermal protection systems, while full scale high fidelity simulations remain computationally demanding for early design phases. A numerical investigation of a supersonic rocket plume impinging on a flat surface is performed using two-dimensional axisymmetric Reynolds Averaged Navier-Stokes simulations. The compressible flow is modeled with the $k-\omega$ SST turbulence model, including convective heat transfer. A parametric study is conducted by varying the nozzle to pad distance under representative operating conditions of a reusable methane fueled rocket engine. Based on the numerical database, a simplified engineering correlation for wall heat flux estimation is derived through dimensional analysis and optimizied using a Particle Swarm Optimization algorithm. The simulations reveal a strong dependance of wall heat flux distribution on plume structure and shock wall interaction mechanisms. The optimized correlation accurately reproduces the main trends and peak values of the numerically predicted heat flux within the investigated range. The proposed correlation provides a computationally efficient tool for preliminary thermal assessments of landing surfaces in reusable launcher applications, bridging the gap between detailed CFD analyses and engineering level design requirements.

Keywords: plume impingement; shock-wall interaction; reusable launcher landing; LOx/CH_4 engine; wall heat flux prediction; particle swarm optimization

1. Introduction

The paradigm shift toward Reusable Launch Vehicles (RLVs) represents one of the most significant technological transformation in modern space transportation. Following the commercial success of SpaceX's Falcon 9 [1], which achieved the first successful orbital class booster recovery and reuse in 2015, the aerospace industry has experienced an accelerating global effort to develop Vertical Takeoff, Vertical Landing (VTVL) systems. These architectures allow to obtain substantial reductions in launch costs, estimated at one order of magnitude compared to expendable systems [2,3] , while simultaneously increasing the number of delivered launches and enabling more sustainable access to space. European initiatives, notably the Prometheus engine and Themis demonstrator programs led by the European Space Agency (ESA) and ArianeGroup, represent the effort toward propulsion systems explicitly designed for reusability [4]. One of the most important point for the operation of reusable launchers is the controlled descent and precision landing phase, during which retro-propulsion is employed to decelerate the returning first stage from supersonic velocities. This maneuver introduces

 doi:10.20944/preprints202603.1386.v1

a complex aerothermal environment characterized by intense plume-surface interactions that generate extreme thermal and mechanical loads on landing infrastructure [5,6]. Unlike traditional launch pad configurations designed to withstand brief ignition transients, reusable landing platforms must endure repeated exposure to high-velocity, high-temperature exhaust jets impinging directly upon their surfaces. For this reason, understanding and accurately predicting these thermal loads is crucial for the development of robust Thermal Protection Systems (TPS) and to ensure structural integrity across multiple reuse cycles.

Recent investigations into retro-propulsion aerothermodynamics have revealed the complex flow physics governing plume-vehicle and plume-surface interactions. Ecker et al. [7] performed numerical studies on the RETALT configurations, demonstrating that thermal loads during supersonic retro-propulsion are primarily driven by plume impingement on the vehicle base and sidewalls, with peak heat fluxes reaching 20 kW/m^2 under specific flight conditions. Similarly, aerothermal characterization of the CALLISTO demonstrator [8] highlighted the critical influence of angle of attack and engine throttling on surface heat flux distributions, emphasizing the need for detailed computational fluid dynamics (CFD) databases to support trajectory design and TPS sizing. These studies consistently indicate that the interaction between exhaust plumes and solid boundaries generates non-uniform, highly localized thermal loads significantly exceeding those encountered during ascent [6,9].

The physical mechanisms underlying jet impingement heat transfer have been extensively studied in the broader heat transfer literature. Zuckerman and Lior [10] provided a comprehensive review of jet impingement physics, identifying the Reynolds number (Re), Prandtl number (Pr) and nozzle-to-pad distance ($d_{nozzle-pad}$) as governing non-dimensional parameters. To take into account the effects of these three non-dimensional parameters simultaneously for subsonic and moderately supersonic jets, the Nusselt number (Nu) can be considered because it can be expressed by a class of empirical correlations of the form $Nu = f(Re, Pr, d_{nozzle-pad})$ [11,12], yet their applicability to rocket plume scenarios, characterized by extreme temperatures ($> 3000\ K$), high Mach numbers (> 2.5) and multi-species reacting flows, remains limited. Moreover, the presence of shock structures, stagnation bubbles and recirculation zones in underexpanded rocket exhausts introduces additional complexities not captured by classical impingement correlations [13,14].

Recent advances in turbulence modeling have enabled high-fidelity simulations of these phenomena. The Reynolds Averaged Navier-Stokes (RANS) approach, coupled with two equations turbulence models such as $k-\omega$ SST, has proven to be effective in detecting wall-bounded flows with strong pressure gradients and shock-boundary layer interactions [15,16]. Numerical studies on plume impingement during rocket landing have demonstrated that RANS based CFD can reliably predict pressure distributions, temperature fields and convective heat fluxes, provided that appropriate mesh resolution and turbulence modeling strategies are employed [9,17]. Nevertheless, the computational burden of high-fidelity simulations, particularly for parametric studies considering multiple standoff distances, thrust levels and atmospheric conditions, justifies the development of reduced order models and engineering correlations suitable for rapid design iterations.

To fill the gap between computationally intensive CFD and practical design needs, optimization algorithms have been increasingly employed to derive simplified heat transfer correlations from numerical datasets. Particle Swarm Optimization (PSO), a heuristic method inspired by collective biological behavior [18], has demonstrated particular effectiveness in solving non-linear, multi-parameter regression problems across various engineering applications. In heat transfer contexts, PSO has been successfully applied to optimize heat exchanger designs [19,20], calibrate thermal models [21] and identify optimal operating parameters [22,23]. Its robustness in navigating complex search spaces without requiring gradient information makes it well-suited for correlating turbulent heat transfer data, where analytical relationships do not represent a viable solution.

The present study addresses the critical knowledge gap in predicting plume induced thermal loads on landing platforms for LOx/CH_4 reusable launchers. Specifically, this work investigates the thermal environment generated by the Prometheus engine during terminal descent and landing. The

 doi:10.20944/preprints202603.1386.v1

Prometheus is a medium thrust class engine ($\sim$ 1000 kN) based on a gas-generator cycle operating at 100 bar chamber pressure and an optimal mixture ratio of 3.5 [4] and represents a cornerstone of Europe's future launcher architecture. Methane offers distinct advantages over hydrogen, including higher density (enabling compact storage), reduced thermal gradients, elimination of hydrogen embrittlement concerns and simplified storage at 112 K versus 20 K for LH_2 [24,25].

Through a systematic combination of high-fidelity CFD simulations, dimensional analysis and PSO based correlation oprimization, this research aims to: (1) characterize the complex flow structures and thermal fields arising from supersonic plume impingement at various nozzle-to-pad distances; (2) quantify the influence of standoff distance and numerical scheme order on peak thermal and mechanical loads; (3) develop a simplified Nusselt based correlation expressing surface heat flux as a function of Reynolds, Prandtl numbers and standoff distance optimized via PSO to minimize residuals against CFD predictions. The resulting correlation is intended to provide preliminary design estimates with acceptable engineering accuracy while reducing computational cost by several orders of magnitude compared to full CFD analyses.

The paper is organized as follows: Section 2 describes the numerical methodology, including governing equations, turbulence modeling, computational domain configuration and details the PSO-based correlation development and validation; Section 3 presents the effects of the numerical discretization accuracy, the parametric simulation results across multiple standoff distances and the outcomes of the wall heat flux prediction by means of the PSO-optimized correlation; Section 4 provides concluding remarks and recommendations for future work. .

2. Materials and Methods

2.1. Engine Configurations and Operating Conditions

The LOx/CH_4 engine configuration considered for the objectives of the present study is the Prometheus engine that represents a medium thrust class propulsion system developed by Ariane-Group in collaboration with ESA as part of Europe's reusability roadmap [4]. This engine employs a gas-generator cycle operating at a chamber pressure of approximately 100 bar, with an optimal mixture ratio (O/F) of 3.5, delivering a vacuum thrust in the range of 1000 kN. The propellant couple employed for the considered engine is liquid oxygen and methane (LOx/CH_4), because of their favorable density, storability and compatibility with reusable operations compared to traditional liquid oxygen and hydrogen (LOx/LH_2) systems.

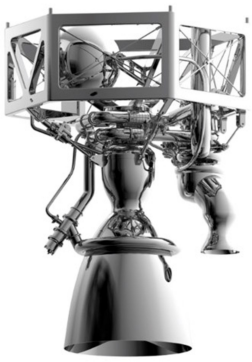

Figure 1. Prometheus engine [26].

For the landing phase simulation, the Prometheus engine has been modeled at 38% throttle to represent realistic descent conditions. By using CIRA in-house design codes that takes in input chamber pressure and geometric expansion ratio of the nozzle it has been possible to rebuild the geometry of the combustion chamber and of the nozzle, guaranteeing that the performances delivered are exactly the same of the considered engine. The chemical composition of the combustion gases has been derived from NASA's CEA software, assuming frozen flow downstream of the combustion

 doi:10.20944/preprints202603.1386.v1

chamber, a resonable assumption given the short residence times in the nozzle expansion section. The species considered from the methane and liquid oxygen reaction are not all of them, but only the ones whose molar fraction exceed 10^{-5}. Table 1 reports the chemical composition of the combustion products considered for the simulation of the Prometheus engine.

Table 1. Chemical composition of the combustion products in terms of molar fractions considered for the simulation of the Prometheus engine.

Species	Molar fraction
CO	0.2226
CO_2	0.25984
H_2	0.00718
H_2O	0.38957
O	0.00994
OH	0.05925
H	0.00118
HO_2	0.00018
O_2	0.04686

The simulations have been performed by considering multiple nozzle to pad distances (indicated with $d_{nozzle-pad}$) to be able to capture the evolution of plume-surface interaction physics, spanning from near contact conditions to moderate separation scenarios relevant to practical landing operations. In particular, 4 nozzle to pad distances have been considered: $d_{nozzle-pad} = 1\ m,\ 5\ m,\ 10\ m,\ 15\ m$. The impingement surface has been modeled as a flat, isothermal wall at a constant temperature of 300 K, representative of steel or refractory landing pad materials before significant thermal transients develop.

2.2. Computational Domain, Boundary Conditions and Mesh Generation

In the framework of the numerical simulations performed in this study, a two-dimensional computational domain based on axial simmetry has been defined that allows to significantly reduce computational burden while capturing the essential physics. While this approach does not resolve three-dimensional effects like asymmetric shock oscillations or large scale coherent structures, previous validation studies have shown that axysimmetric RANS models provide reliable predictions of mean flow quantities, pressure distributions and time averaged heat fluxes for impinging jet configurations [13,14]. The computational domains adopted for the simulations of the Prometheus engine plume are reported in Figure 2(a). For the sake of clarity, only the domain corresponding to a nozzle to pad distance of $d_{nozzle-pad} = 15\ m$ is explicitly depicted; the dashed lines indicate the truncation locations of the computational domain associated with the other distances considered. For each case, the domain is truncated at the plane corresponding to the selected nozzle to pad distance. Figure 2(b) is a close up of the domain in the nozzle region.

As it is possible to appreciate in Figure 2, the boundary conditions have been specified as follows. At the nozzle inlet (combustion chamber exit), a prescribed mass flow inlet with a specified mass flux has been set ($\dot{m} = 101.7\frac{kg}{s}$) together with the total temperature ($T_0 = 3473.43K$), the chamber pressure ($p_c = 37bar$) and the species mass fractions from CEA and reported in Table 1. Turbulence intensity has been set to 5% with a hydraulic diameter equal to the chamber diameter, consistent with high velocity combustion chamber flows. On the impingement wall, a no slip condition with a fixed temperature ($T_{wall} = 300K$) has been set. Ambient boundaries (far field) have been treated as pressure outlets with static pressure $p_\infty = 1bar$ (sea level condition) and temperature $T_\infty = 300K$. The axis of simmetry enforced zero radial velocity and zero radial gradients of all scalar quantities. The nozzle wall was modeled with a no slip condition with temperature set to 300K. A synoptic overview of the boundary conditions is reported in Table 2.

 doi:10.20944/preprints202603.1386.v1

Table 2. Boundary conditions adopted.

Region	BCs
Nozzle inlet	Mass flow inlet $\dot{m} = 101.7 \frac{kg}{s}$ $p_c = 37 bar$ $T_0 = 3473.43 K$ $O/F = 3.5$
Wall Nozzle	No slip $T_{wall} = 300 K$
Axis	Simmetry
Ambient boundaries	Pressure Outlet $p_\infty = 1 bar$ $T_\infty = 300 K$
Impinging wall	No slip $T_{wall} = 300 K$

Three mesh densities have been generated to assess grid independence: approximately 21375 cells (coarse), 85250 cells (medium) and 341000 cells (fine). All meshes featured structured quadrilateral elements with refined clustering in three critical regions: the nozzle exit plane where expansion waves and shock structures originate, the plume ambient interface characterized by strong shear layers and the impingement wall boundary layer where convective heat transfer peaks. The first cell center has been placed 0.4 mm from solid boundaries, yielding y^+ values ranging from $20 \div 200$ for the fine mesh, around 190 for the medium mesh and exceeding 400 for the coarse mesh. These distributions align well with $k - \omega$ SST turbulence modelling requirements. Grid convergence was evaluated by comparing wall pressure and surface heat flux distributions across the three densities. The maximum relative deviation in peak heat flux between medium and fine grids was 0.68%, compared to 0.92% between coarse and fine grids. Wall pressure distributions showed a 3.3% discrepancy (medium vs. fine) and 5.7% (coarse vs. fine). Combined with the y^+ considerations, these metrics confirmed that the fine mesh provided sufficient spatial resolution for accurate thermal load prediction, so this density (341000 cells) has been adopted for all subsequent parametric studies.

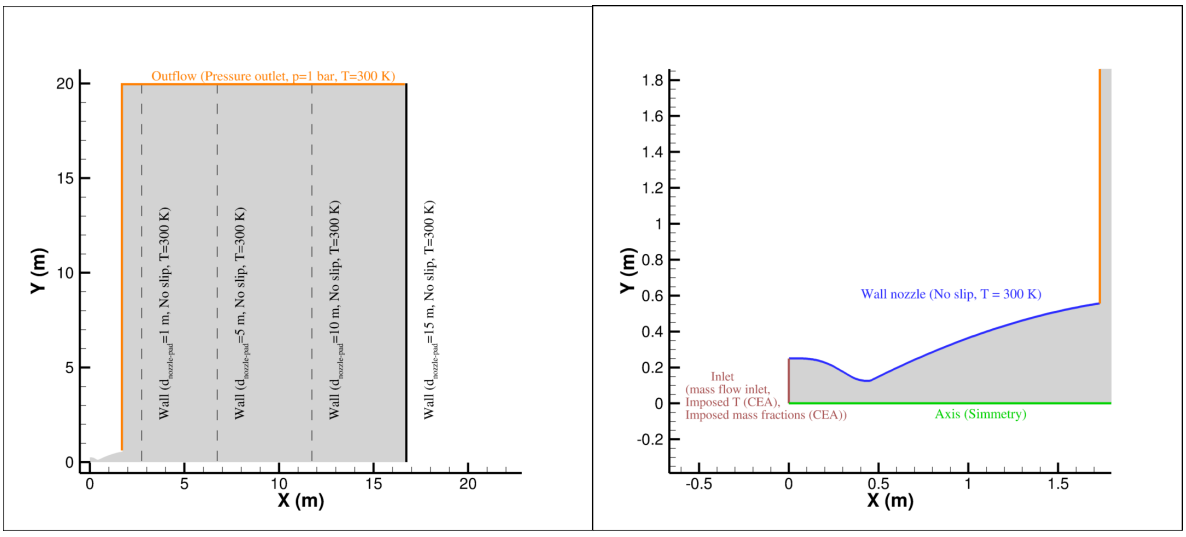

(**a**) (**b**)

Figure 2. (a): Computational domain and boundary conditions considered for the simulation of the plume of the Prometheus engine impinging on pads at four different distances . **(b)**: Close up near the nozzle of the computational domain and boundary conditions imposed.

 doi:10.20944/preprints202603.1386.v1

2.3. Governing Equations and Turbulence Modelling

The exhaust plume behavior has been described using the compressible Reynolds-Averaged Navier-Stokes (RANS) equations, which decompose instantaneous flow quantities into mean and fluctuating components. This approach enables turbulent flow simulation at computational costs several orders of magnitude lower than Direct Numerical Simulation or Large Eddy Simulation. For turbulence modelling, the $k-\omega$ Shear Stress Transport (SST) model has been adopted. The transport equations for turbulent kinetic energy (k) and specific dissipation rate (ω), along with the turbulent viscosity formulation, follow the standard SST implementation detailed in [27–30]. Thermophysical properties have been treated as temperature dependent using polynomial curve fits from NIST databases [31]. The ideal gas equation of state was employed, with mixture-averaged properties computed by means of kinetic theory for the nine species combustion gas mixture.

2.4. Numerical Solution Procedure

Simulations were conducted using ANSYS Fluent 2025R2, a widely validated commercial CFD solver employing finite volume discretization. A pressure based coupled algorithm has been used, which solves momentum and pressure-correction equations simultaneously, offering enhanced robustness and faster convergence for compressible flows compared to segregated schemes. Two sets of simulations were performed to evaluate how spatial discretization accuracy affects the predicted thermal loads:

- First-order simulations used first order upwind interpolation for all spatial gradients (pressure, density, momentum, energy, turbulence variables). This scheme offers excellent numerical stability and it is not affected by non physical oscillations near discontinuities like shocks, but introduces significant numerical diffusion that artificially smooths gradients.
- Second-order simulations employed a second order upwind scheme for all transport equations. Higher order discretization reduces numerical diffusion and provides sharper resolution of shock structures, velocity gradients and thermal boundary layers, essential for accurate heat flux prediction in high speed flows.

Convergence was monitored by means of residual histories (scaled residuals below 10^{-6} for continuity and momentum, 10^{-8} for energy) and through stabilization of integral quantities like mass flow rate at the nozzle inlet and total pressure force on the impingement plate. All simulations ran in steady state mode, which is reasonable given that the primary flow structures (Mach disk, stagnation bubble) exhibit relatively low frequency unsteadiness that does not significantly affect time averaged surface heat fluxes.

2.5. Particle Swarm Optimization for Correlation Development

While CFD simulations offer detailed insight into plume-surface interactions, their computational expense, often tens to hundreds of CPU hours per case, limits their usefulness during preliminary design or parametric sensitivity studies. This motivates the development of simplified engineering correlations that enable rapid thermal load estimation without full numerical solutions. Classical dimensional analysis suggests that the Nusselt number for impinging jets can be expressed as a power law function of Reynolds and Prandtl numbers [10,11]:

$$Nu = C \cdot Re^{a} \cdot Pr^{b} \tag{1}$$

where C, a, and b are empirical coefficients determined from experimental or numerical data. However, identifying optimal values for these coefficients from CFD datasets is challenging, particularly when the underlying physics shows strong dependencies on multiple parameters like nozzle to pad distance, shock structure and recirculation effects.

To solve the problem of identifying the optimal values for the coefficients in the Nusselt correlation, the Particle Swarm Optimization (PSO) algorithm has been adopted. The PSO is a population based metaheuristic algorithm inspired by collective behaviour in biological swarms like bird flocks and

 doi:10.20944/preprints202603.1386.v1

fish schools, originally developed by Kennedy and Eberhart in 1995 [18]. PSO has proven to be particularly effective in heat transfer applications, including design optimization of shell and tube heat exchangers, plate fin exchangers and thermal model calibration, often outperforming genetic algorithms in convergence speed and solution quality for continuous design variables [19–21]. The PSO algorithm works by initializing a population (swarm) of N particles, each representing a candidate solution defined by a position vector $\underline{X} = [C, a, b]$ in three dimensional parameter space. Each particle also gets assigned a velocity vector $\underline{V}$ that governs its movement through the search domain. During initialization, particle positions are randomly distributed within predefined bounds:

$$X_i = X_{min} + (X_{max} - X_{min}) \cdot rand() \tag{2}$$

where $rand()$ generates a uniform random number between 0 and 1. Initial velocities are similarly randomized to ensure broad exploration of the parameter space.

Solution quality is evaluated using an objective function J, formulated here as the sum of squared residuals between the Nusselt numbers predicted by CFD simulations and by correlation estimates:

$$J_z^p = \sum_{i=1}^{N_{points}} (Nu_{CFD,i} - Nu_{corr,i})^2 \tag{3}$$

where $Nu_{CFD,i}$ is the local Nusselt number from CFD simulation at the position i, $Nu_{corr,i}$ is the corresponding value computed using the correlation with the current particle's coefficients and N_{points} is the number of spatial locations along the impingement surface. This formulation ensures the optimization minimizes discrepancies across the entire radial Nusselt number distribution, not just peak values. At each iteration p, particles update their velocities and positions based on three behavioral components: inertia (tendency to mantain current trajectory, weighted by C_1), cognitive attraction toward the particle's own historically best position (namely Personal Best (PB), weighted by C_2) and social attraction toward the globally best position found by the entire swarm (namely Global Best (GB), weighted by C_3). The velocity update equation is:

$$V_z^{p+1} = C_1 \cdot V_z^p + C_2 \cdot rand() \cdot \left(PB_z^p - X_z^p\right) + C_3 \cdot rand() \cdot \left(GB^p - X_z^p\right) \tag{4}$$

particle positions the update according to:

$$X_z^{p+1} = X_z^p + V_z^{p+1} \tag{5}$$

If an updated position violates the predefined bounds (X_{min}, X_{max}). it gets corrected by assigning the corresponding boundary value. After position updates, the objective function is re-evaluated for each particle. If a particle's current fitness J_z^{p+1} beats its previous personal best, the Personal Best updates accordingly. Similarly, the Global Best updates if any particle achieves fitness better than the current swarmwide optimum.

This iterative process continues until a stopping criterion is met, typically either a maximum number of iterations or negligible improvement in global best fitness over successive generations. The PSO algorithm has demonstrated ability to mantain allowable error tolerances while avoiding premature convergence to local minima.

For heat transfer correlation problems, PSO offers several practical advantages over gradient based optimization: it does not require analytical derivatives of the objective function, exhibits robustness to noisy data (inherent in turbulent CFD solutions) and efficiently explores multi modal search spaces without excessive sensitivity to initial guesses [23]. Recent applications of PSO and related Bayesian optimization techniques to CFD based calibration have shown that metaheuristic algorithms can successfully identify optimal turbulence model coefficients and heat transfer correlation parameter, often achieving better predictive accuracy than manually tuned values [32,33].

In this work, PSO has been implemented with the following configuration: swarm size $N = 30$ particles, maximum iterations $p_{max} = 200$, inertia weight factor $C_1 = 0.7$, cognitive weight factor

 doi:10.20944/preprints202603.1386.v1

$C_2 = 1.4$ and social weight factor $C_3 = 1.4$. These values align with recommended settings from the PSO literature. The search domain for each coefficient was defined based on typical ranges reported for impinging jet correlations, in particular: $0.001 \leq C \leq 0.1$, $0.5 \leq a \leq 1.0$ and $0.3 \leq b \leq 0.8$. For the development and optimization of the correlation, the following strategy has been adopted: the Reynolds and Prandtl numbers obtained from the CFD simulation at a nozzle-pad distance of 15 m were used to calibrate the coefficients C, a, b in Equation 1. The optimization was performed by minimizing the error between the predicted Nusselt number and the CFD results at this reference distance. Once the optimal coefficients were determined, the resulting Nusselt number correlation was applied to predict the thermal fluxes at different nozzle-pad distances. This approach allows for the validation of whether a single CFD simulation at one distance can provide a sufficiently accurate correlation for predicting heat fluxes at other distances, thereby reducing the computational cost associated with multiple CFD analyses.

3. Results

3.1. Effects of the Numerical Discretization Accuracy

In order to evaluate the impact of numerical discretization accuracy on the simulation outcomes, a comparative analysis has been carried out by considering first and second order spatial schemes. First order schemes are generally more stable and robust in terms of convergence, particularly in the presence of steep gradients and shock waves. However, this stability comes at the cost of elevated numerical diffusion, which leads to a marked smoothing of essential flow features. The most important consequences include the damping of shock structures, the underprediction of velocity gradients and the artificial thickening of thermal boundary layers. As a result, critical quantities such as wall heat fluxes and stagnation point pressures are often underestimated, potentially compromising the fidelity of the thermal load assessment. On the contrary, second order schemes offer significantly improved resolution of spatial gradients, allowing for a more accurate representation of fluid dynamic structures, including the Mach disks, shear layers and stagnation regions. With a higher order spatial discretization it is possible to preserve and capture sharper profiles of velocity, pressure and temperature, leading to a more faithful reconstruction of the flow field. For these reasons, first order schemes may suffice for preliminary analyses or conservatives estimates while second order schemes are indispensable for resolving the complex physics of plume impingement and for ensuring high fidelity predictions of the thermal loads experienced by the landing platform. In the following, for brevity's sake, the comparisons of the results obtained with first and second order schemes for the case in which the distance between the nozzle and the pad is $d_{nozzle-pad} = 5\ m$ are reported, but for all the other distances same considerations apply. In Figure 3, a comparison between the heat flux distributions on the pad ($d_{nozzle-pad} = 5\ m$) obtained with first and second order schemes is presented; it is possible to observe that the peak heat flux is higher in the second order solution and that it is located on the axis of the nozzle (the center of the impingement region on the pad), on the contrary in the first order solution the peak is predicted to be located with a 0.25 m displacement with respect to the nozzle axis. These differences suggest the effectiveness of higher order accuracy schemes in detecting flow field structures, as it is possible to appreciate in Figure 4, where a shadowgraph visualization of the flow field is compared between first and second order solution; the latter shows a more defined shock structure and the presence of a normal shock right over the pad with a standoff distance of about 1 m, not detected by first order solution. Furthermore, in Figure 5 the contour plot of the static pressure shows the overexpanded nature of the plume, how the second order solution detects the plume structure more sharply for a longer distance with respect to the first order solution because of numerical diffusion and how the first order solution underpredicts the pressure increase downstream of a Mach disk. All of these differences in the plume structure reflect on the distribution of total pressure and total temperature on the pad, as shown in Figure 6 and Figure 7, respectively. In the following, the second order solutions will be presented and discussed, since the flow field predicted by higher order accuracy schemes appears to be more detailed.

 doi:10.20944/preprints202603.1386.v1

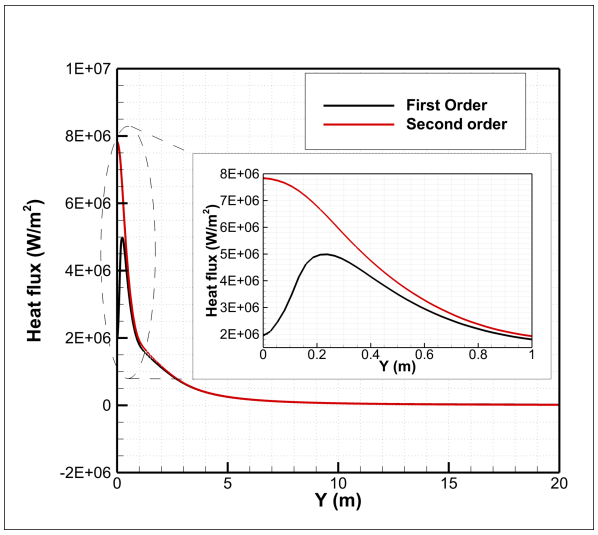

Figure 3. Heat flux distribution on the pad relative to first and second order schemes ($d_{nozzle-pad} = 5\ m$).

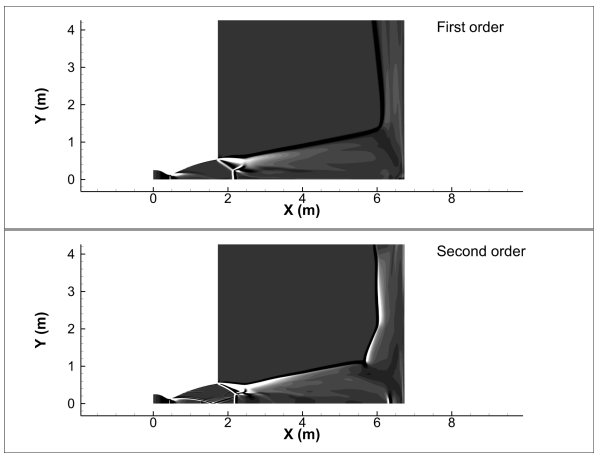

Figure 4. Comparison of the Shadowgraph visualization of the flowfield obtained with first and second order discretization schemes ($d_{nozzle-pad} = 5\ m$).

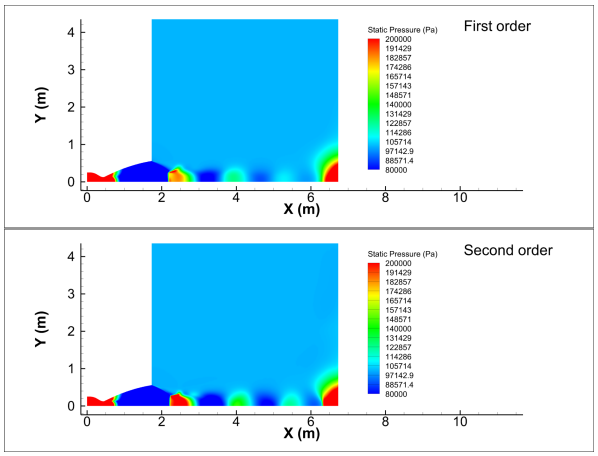

Figure 5. Comparison of the static pressure field obtained with first and second order discretization schemes ($d_{nozzle-pad} = 5\ m$).

Preprints.org (www.preprints.org) | NOT PEER-REVIEWED | Posted: 19 March 2026 doi:10.20944/preprints202603.1386.v1

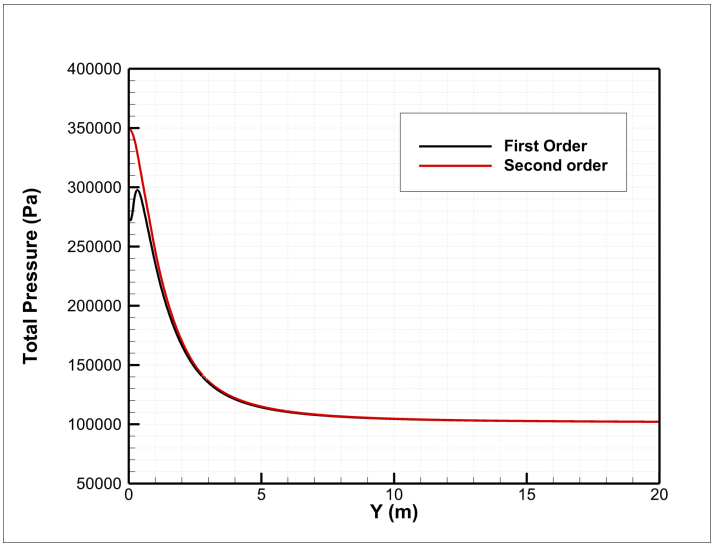

Figure 6. Comparison of total pressure distribution on the pad obtained with first and second order discretization schemes ($d_{nozzle-pad} = 5\ m$).

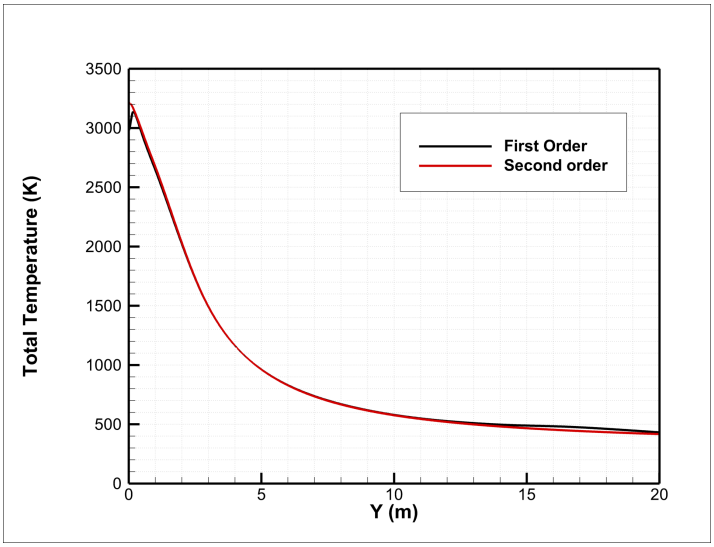

Figure 7. Comparison of total temperature distribution on the pad obtained with first and second order discretization schemes ($d_{nozzle-pad} = 5\ m$).

3.2. The Effect of Nozzle to Pad Distance

The numerical simulations revealed complex flow physics dominated by the typical shock wave patterns of overexpanded rocket nozzles. An investigation about the effect of the structure of the plume and about the thermal and mechanical field established on the pad has been carried out by considering four nozzle to pad distances. For the $d_{nozzle-pad} = 15\ m$ case, the plume developed quite freely without significant interference with the pad, as it can be seen in Figure 8 (a). The first Mach disk formed at approximately 1.07 m from the nozzle exit, with a clearly visible triple point where the normal shock, incident oblique shock and reflected shock converge. As the nozzle approaches the pad (Figure 8 (b,c)), the shock structure begins to interact with the pad. An interesting phenomenon emerged: the triple point shifted away from the nozzle axis and moved upstream toward the nozzle exit. This behaviour is due to the backpressure effect imposed by the presence of the pad. The subsonic region downstream of the normal shock expanded laterally and the Mach disk weakened progressively as the nozzle approached the pad. The most important change in plume structure and interaction with the pad occured at $d_{nozzle-pad} = 1\ m$ (Figure 8 (d)). In this case the entire region downstream of the normal shock became subsonic, creating a large stagnation zone directly ahead of the impingement

 doi:10.20944/preprints202603.1386.v1

point. The flow pattern fundamentally differed from the other cases because instead of a well defined shock structure, the simulation showed a broad, weakened normal shock positioned very close to the nozzle exit (approximately 0.7 m).

One of the most significant findings concerns the formation of a stagnation bubble that appeared prominently at $d_{nozzle-pad} = 1\ m$. Figure 9 shows the detailed velocity field near the wall for these cases $d_{nozzle-pad} = 5\ m$, where the stagnation bubble has not yet developed and $d_{nozzle-pad} = 1\ m$, where the recirculation pattern is clearly visible. The physical mechanism behind this phenomenon is due to the fact that when the jet impinges on the pad, the flow behind the normal component of the Mach disk experiences much higher total pressure loss than the flow passing through the oblique shocks. This pressure differential creates a central region characterized by low pressure that cannot sustain direct impingement, forcing the high velocity flow to deflect radially outward before reaching the pad centerline and this deflecting effect enhance when the nozzle approaches the pad.

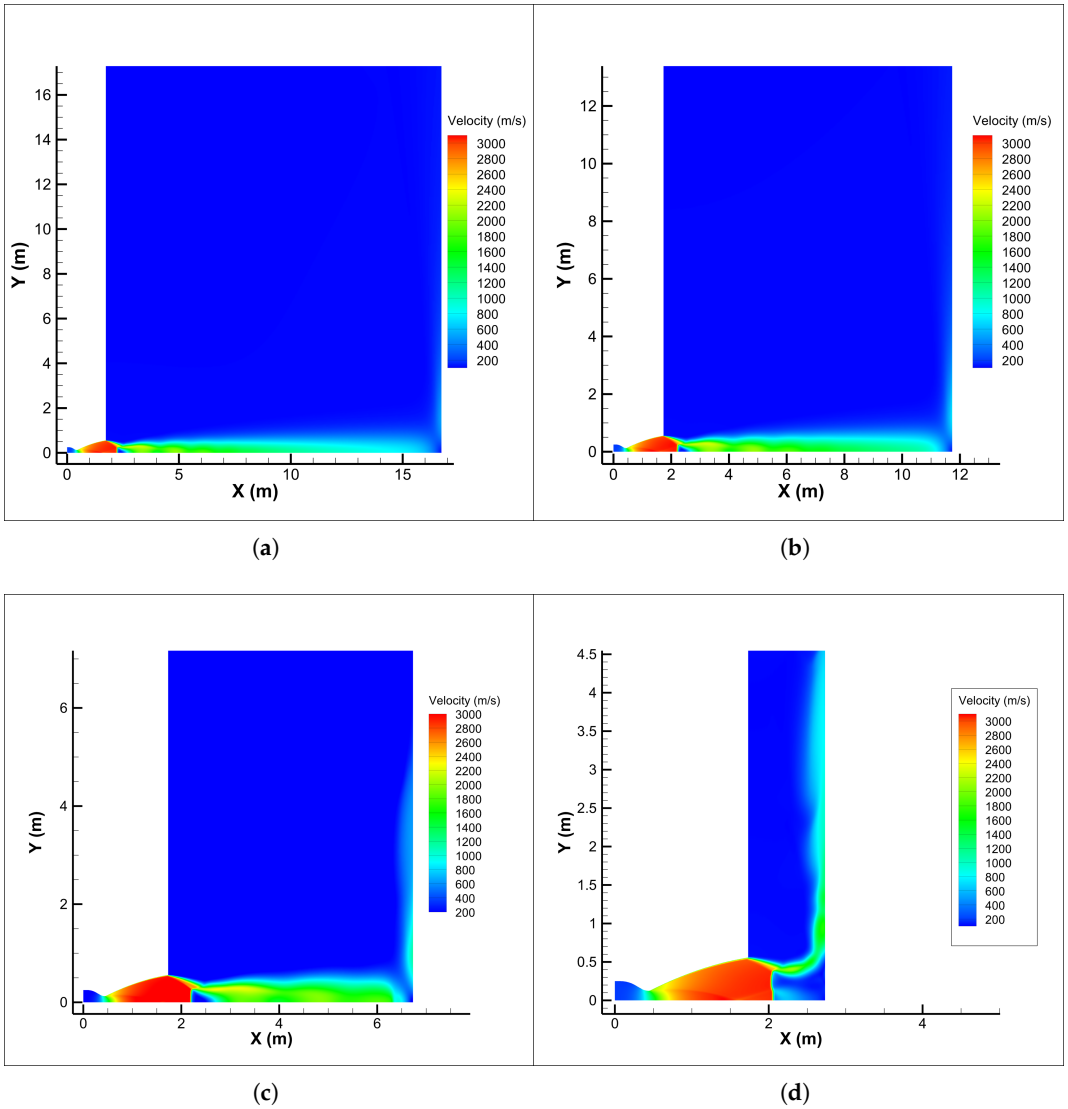

Figure 8. Velocity contour plots for **(a)** $d_{nozzle-pad} = 15m$ case, **(b)** $d_{nozzle-pad} = 10m$ case, **(c)** for $d_{nozzle-pad} = 5m$ case, **(d)** for $d_{nozzle-pad} = 1m$ case.

 doi:10.20944/preprints202603.1386.v1

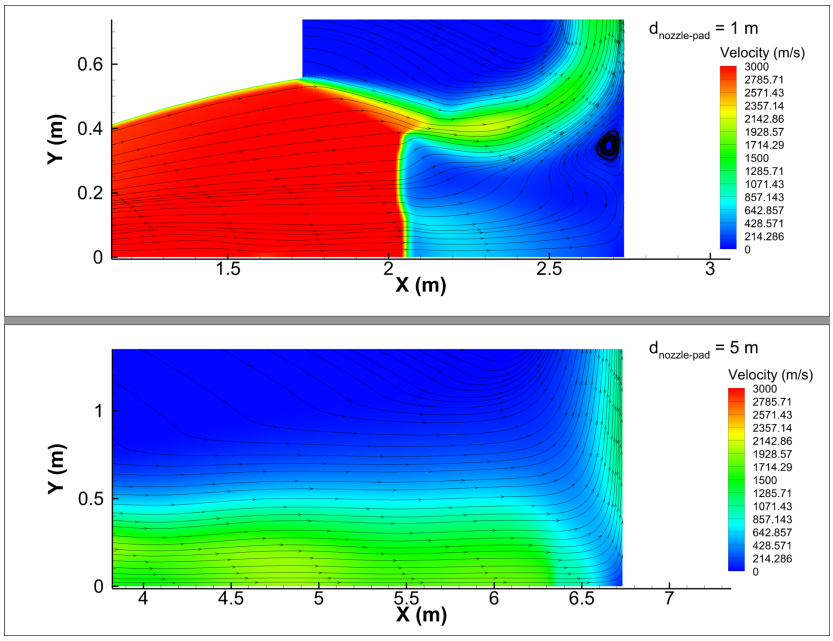

Figure 9. Close up of the velocity contour plot and streamlines for the distances $d_{nozzle-pad} = 1\ m$ and $d_{nozzle-pad} = 5\ m$.

The wall pressure distribution reported in Figure 10 quantify this behaviour. For $d_{nozzle-pad} = 1\ m$, the static pressure profile exhibits a series of local minima and maxima which testify the presence of the stagnation bubble. The peak pressure is shifted radially outward to about 0.6 m from the axis, where the deflected jet actually impacts the surface. At $d_{nozzle-pad} = 5\ m$ the stagnation bubble is present, but it is starting to develop and grow and so the pressure peak occurs at the centerline and the profile is monotonic. As the distance $d_{nozzle-pad}$ increases to 10 m and beyond, the stagnation bubble disappears entirely. The wall pressure distribution is always monotonic, with the maximum occurring directly on the pad centerline, the classical behaviour expected for impinging jets without strong shock surface interaction.

The heat flux distributions reveal the same physics. Figure 11 shows the wall heat flux for all the cases. For $d_{nozzle-pad} = 15\ m$ and $d_{nozzle-pad} = 10\ m$, where no stagnation bubble forms, the heat flux exhibits a clear peak at the stagnation point, located at the pad centerline, reaching approximately 1 MW/m^2 and 3.1 MW/m^2, respectively. This behaviour aligns with classical impinging jet theory: the maximum heat transfer occurs where the flow stagnates directly, driven by the thin boundary layer. For the case $d_{nozzle-pad} = 5\ m$ the peak value still occurs at the pad centerline and it reaches the highest value observed in all the simulations, 7.8 MW/m^2. In all the cases presented until now, the wall heat flux is monotonically decreasing. On the contrary, the $d_{nozzle-pad} = 1\ m$ case shows a different pattern characterized by the presence of the stagnation bubble revealed by a profile with one peak ($\sim 7.5\ MW/m^2$) located at 0.6 m from the pad centerline and two relative maxima, similarly to what happened for the pressure distributions. The most important thing to notice is that the maximum heat flux does not occur when the distance between the nozzle and the pad is the minimum considered ($d_{nozzle-pad} = 1\ m$) but when $d_{nozzle-pad} = 5\ m$ because dynamic effects and turbulence enhance the heat transfer. A comparison of the distribution of the turbulent viscosity (μ_t) is reported in Figure 12. By comparing the distributions of wall heat flux (Figure 11) and turbulent viscosity (Figure 12) it is possible to notice that, although the turbulent viscosity reaches its maximum value at $d_{nozzle-pad} = 10\ m$, the corresponding wall heat flux does not peak at this distance. This apparent discrepancy highlights the fact that turbulent viscosity alone is not a direct predictor of wall heat transfer. At larger distances ($d_{nozzle-pad} = 15\ m$), the enhanced turbulent mixing occurring upstream of the impingement leads to a partial homogenization of velocity and temperature fields, thereby reducing the thermal gradients at the wall. At intermediate distances ($d_{nozzle-pad} = 5\ m$), turbulence levels are sufficiently high to sustain an energetic wall jet, while the plume still retains strong velocity and temperature gradients

 doi:10.20944/preprints202603.1386.v1

upon impingement. This combination results in steeper near wall temperature gradients and a higher convective heat flux, despite the turbulent viscosity being lower than its maximum value. For the smallest distance ($d_{nozzle-pad} = 1\ m$), strong stagnation effects and turbulence suppression inherent to the $k-\omega$ SST model limit turbulent transport and wall jet development, leading to reduced heat flux.

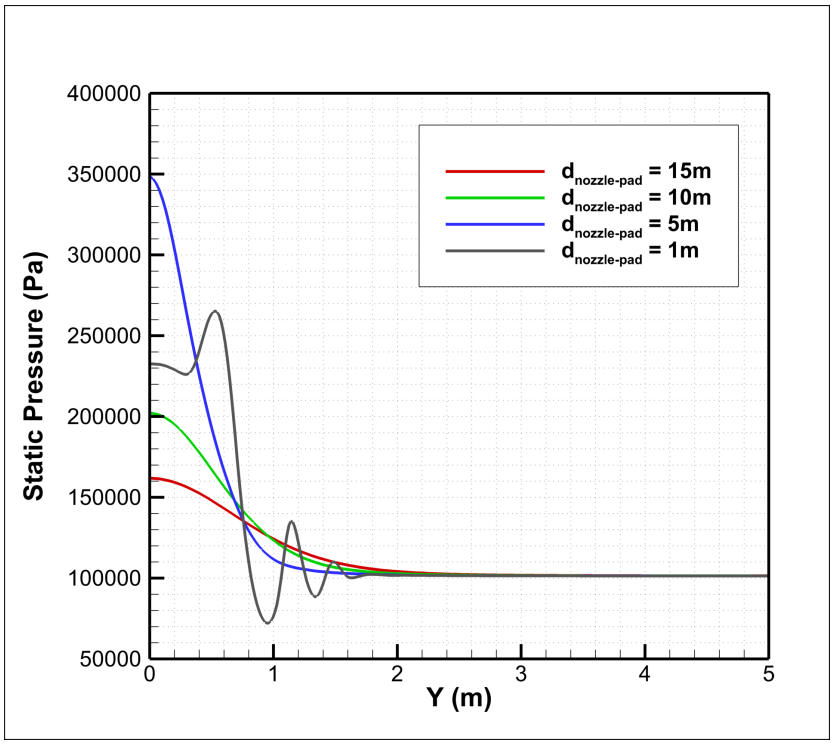

Figure 10. Static pressure distributions on the pad for the four cases.

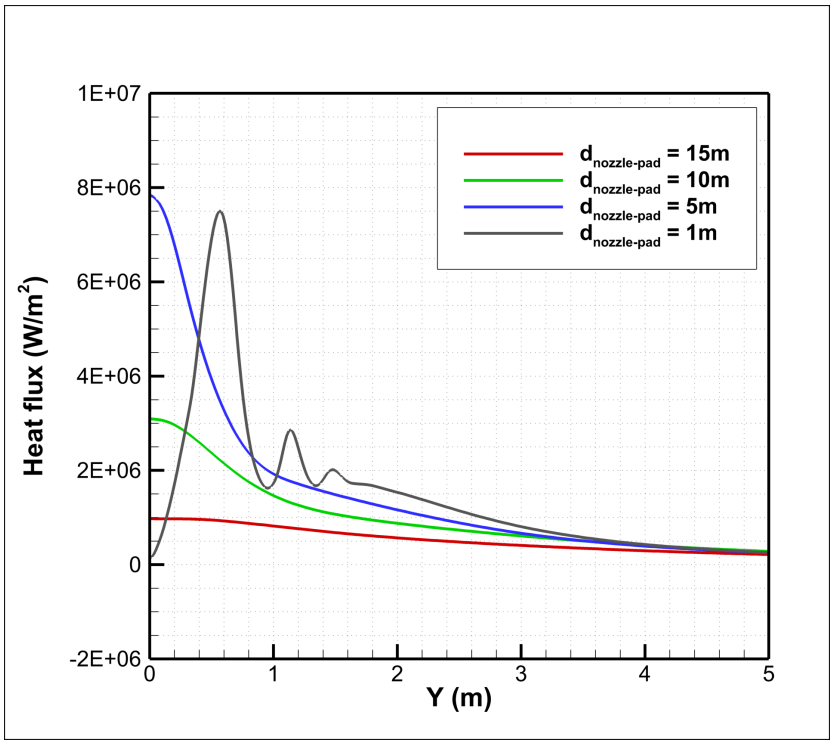

Figure 11. Heat flux distributions on the pad for the four cases.

 doi:10.20944/preprints202603.1386.v1

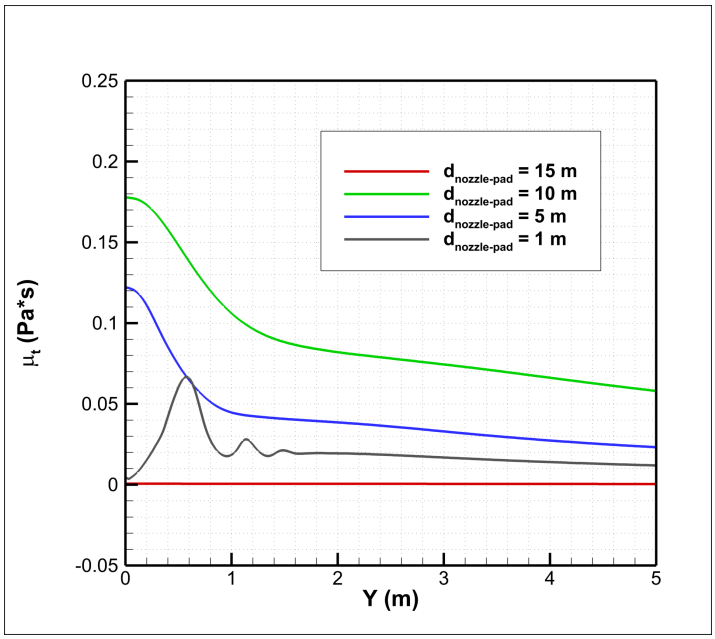

Figure 12. Turbulent viscosity distributions near the pad for the four cases.

3.3. Development of an Optimized Correlation for the Prediction of Wall Heat Flux by Means of PSO

Having established a comprehensive CFD database, an optimized correlation for rapid heat flux estimation has been developed. The objective of this optimization effort is to derive a single correlation that, calibrated using data from just one CFD simulation at a reference stadoff distance $d_{nozzle-pad}$, could reliably predict thermal loads at other distances without requiring additional full scale simulations. This would provide designers with a computationally inexpensive tool for preliminary assessments, while also quantifying the error accumulated when extrapolating the correlation beyond its calibration range.

The particle swarm optimization algorithm has been applied by considering the CFD data relative to the $d_{nozzle-pad} = 15\ m$ case to identify the optimal coefficients C, a, b in the power law relation $Nu = C \cdot Re^a \cdot Pr^b$. This particular distance has been chosen because it represents a regime where the interactions between the plume and the pad are negligible, without strong stagnation bubble effects that could introduce additional nonlinearities. The Reynolds and Prandtl numbers have been extracted from the CFD solution at various positions along the pad outside the boundary layer but within the plume region. For a given location the local velocity, density, viscosity and thermal conductivity have been used to compute Re and Pr and these values were then used to rebuild the Nusselt number distribution over the pad, the convective heat transfer coefficient h_c and the heat flux q''_{corr}.

The resulting correlation for $d_{nozzle-pad} = 15\ m$ took the form:

$$Nu = 0.0103 \cdot Re^{0.9571} \cdot Pr^{0.5642} \tag{6}$$

By comparing the Nusselt number distributions provided by CFD results and PSO in Figure 13 (a) it is possible to notice that the optimized correlation underpredicted the peak value with an error of 5.17% and tracked the radial distribution reasonably well on the pad, predicting the location of the peak with a shift of 1.6 m from the centerline, while the CFD peak is predicted at 0.6 m from the centerline. The convective heat flux coefficient h_c, reported in Figure 13 (b), computed with the Nusselt distribution, also well predicts the CFD prediction with an underprediction of the peak value of 6.48%, with the same shift in peak location. By considering the heat flux rebuilt by means of the optimized Nusselt correlation, shown in Figure 13 (c), there is an underestimation of the peak value of 24.74% with respect to the CFD result and while the peak value location predicted by CFD is on the pad centerline, the PSO predicts the location of this peak with a shift from the centerline of 0.9 m. So, the optimization of the coefficients used in the power-law of the Nusselt number minimized the error

 doi:10.20944/preprints202603.1386.v1

in the prediction of the Nusselt number distribution, but by considering the heat flux rebuilt with these distribution it has been shown that the peak heat flux is underestimated. In a preliminary design phase, a calibration constant can be introduced in the Nusselt number correlation with the objective to obtain a peak value of the heat flux that would be the same of the one predicted by CFD results. To satisfy this condition the calibration constant, named A, must have a value of $A = 1.32$. So the Nusselt number correlation becomes:

$$Nu = 1.32 \cdot 0.0103 \cdot Re^{0.9571} \cdot Pr^{0.5642} \tag{7}$$

With the introduction of the calibration constant, the heat flux distribution on the pad is the one presented in Figure 14, where it is possible to notice that the peak value predicted is the same of the CFD results. The location of the peak is not of fundamental importance because by studying the effect of nozzle to pad distance a shifting of this location has been observed and for the design of the pad it is important to have a reliable prediction of the peak heat flux. For radial positions for which $Y > 2m$ the corrected heat flux distribution overestimates the CFD results.

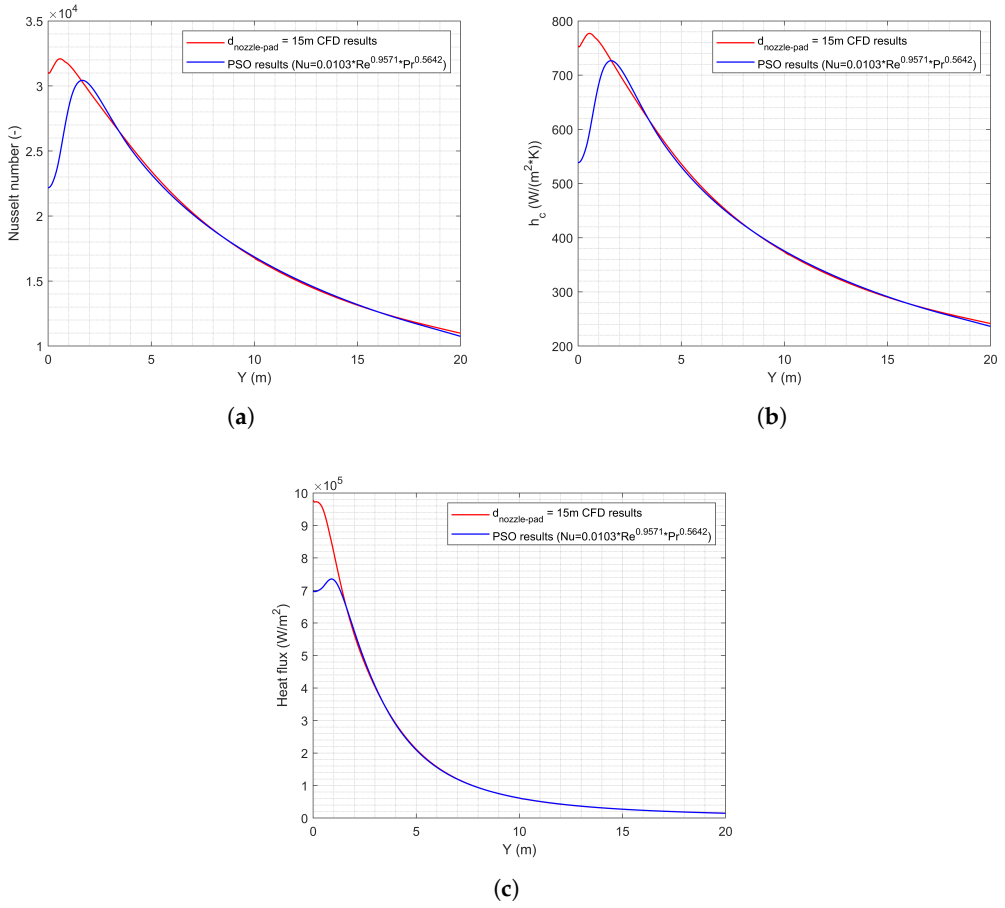

Figure 13. (a) Comparison of Nusselt number distribution on the pad obtained with CFD and PSO for $d_{nozzle-pad} = 15\ m$. **(b)** Comparison of convective heat transfer coefficient distribution on the pad obtained with CFD and PSO for $d_{nozzle-pad} = 15\ m$. **(c)** Comparison of heat flux on the pad obtained with CFD and PSO for $d_{nozzle-pad} = 15\ m$.

 doi:10.20944/preprints202603.1386.v1

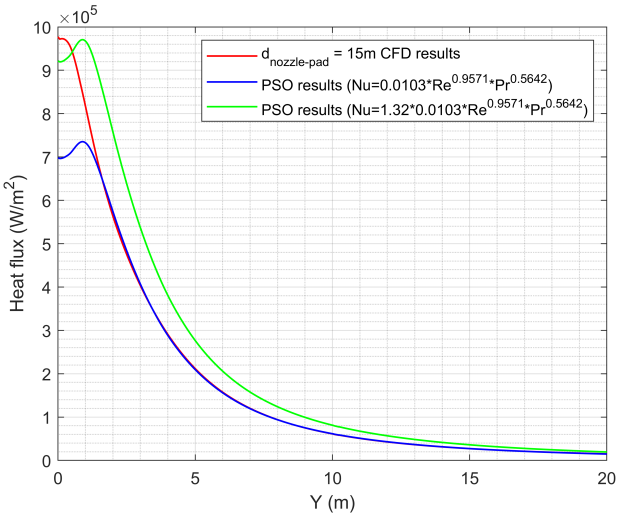

Figure 14. Wall heat flux predicted by CFD results, optimized Nusselt correlation and correction with the calibration constant ($d_{nozzle-pad} = 15m$).

In Figure 15 is reported the comparison of heat fluxes on the pad obtained with CFD and correlations for $d_{nozzle-pad} = 10\ m$. The correlation results reported refer to: the heat flux rebuilt by means of the optimized correlation obtained by considering the $d_{nozzle-pad} = 10\ m$ data ($Nu = 0.0199 \cdot Re^{0.9363} \cdot Pr^{0.3097}$) and the $d_{nozzle-pad} = 15\ m$ corrected correlation (Equation 7). It is possible to appreciate how the heat flux rebuilt by means of the optimized correlation for $d_{nozzle-pad} = 10\ m$ overestimates the peak value with an error of 15.06%, while the prediction offered by Equation 7 is closer to the CFD value, with an error of 7.33%. It is important to notice that both the correlations, for radial positions in which $Y > 1m$, underpredict the heat flux on the pad with respect to the CFD evidence, because the Reynolds and Prandtl numbers drop more steeply than the actual convective transfer does. Since in this region the values of heat flux appear to be way lower then the peak value, it is an acceptable compromise for the objectives of the present work.

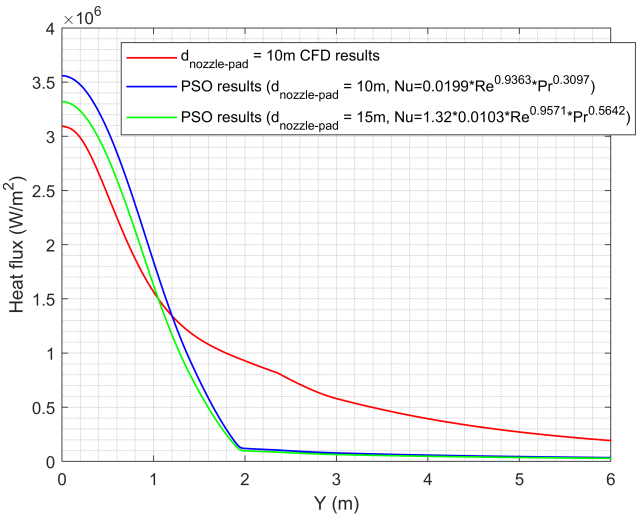

Figure 15. Wall heat flux predicted by CFD results for $d_{nozzle-pad} = 10\ m$, optimized Nusselt correlation for $d_{nozzle-pad} = 10\ m$, correlation obtained with data for $d_{nozzle-pad} = 15\ m$ corrected with calibration constant.

Figure 16 shows the comparison between the heat flux obtained with CFD and with correlations for $d_{nozzle-pad} = 5\ m$ case. Also in this case the optimal correlation for Nusselt number has been found by means of PSO ($Nu = 0.0199 \cdot Re^{0.9214} \cdot Pr^{0.3049}$) by considering the $d_{nozzle-pad} = 5\ m$ data and has been compared with the results obtained with Equation 7, related to $d_{nozzle-pad} = 15\ m$. The prediction of the peak heat flux value offered by using this latter correlation is closer to the CFD

 doi:10.20944/preprints202603.1386.v1

value then the prediction given by the optimized correlation for $d_{nozzle-pad} = 5\ m$ (the prediction errors are 11.72% and 27.30%, respectively). In the end, in Figure 17 the same comparison is shown for the $d_{nozzle-pad} = 1\ m$ case. In this case the optimized correlation obtained by considering the $d_{nozzle-pad} = 1\ m$ data has assumed the form $Nu = 0.0199 \cdot Re^{0.8937} \cdot Pr^{0.3091}$, but by rebuilding the heat flux profile with this correlation it is possible to appreciate that it is always underestimated with respect to the CFD evidence (error on the peak value of 23.51%), on the contrary the rebuilding obtained with Equation 7 overestimates the CFD result (error on the peak value of 15.03%). In the heat flux distribution predicted by any correlation there is no evidence of the presence of the stagnation bubble as previously discussed and as it is visible by the CFD result, where some relative maxima are present. However, this limitation does not undermine the correlations' practical utility. The primary purpose of simplified engineering correlations is not to reproduce the detailed spatial distribution of heat flux with all its local features, but rather to provide a reliable first-order estimate of the maximum thermal loads that is the critical design parameter for sizing thermal protection systems and assessing material limits. From this perspective, the correlations perform well: they predict peak heat flux values with errors generally below 20% and when discrepancies occur, they tend toward conservative overestimation rather than dangerous underprediction. The inability to resolve complex flow features like stagnation bubbles or secondary peaks is an expected consequence of reducing the physics to a simple power law function of two non-dimensional parameters. These local flow structures depend on highly nonlinear shock-wall interactions, recirculation dynamics and turbulence production mechanisms that cannot be fully encoded in Reynolds and Prandtl numbers alone. Capturing such details would require either distance-specific correlations or more sophisticated functional forms (e.g., including $d_{nozzle-pad}$ explicitly or multi-region piecewise formulations) approaches that would compromise the simplicity and computational efficiency that make these tools valuable for preliminary design iterations. For applications requiring accurate spatial resolution of thermal loads, full CFD simulations remain necessary. The correlations developed here serve a complementary role: enabling rapid parametric studies, providing order of magnitude estimates during conceptual design and offering conservative bounds for worst case thermal load scenarios.

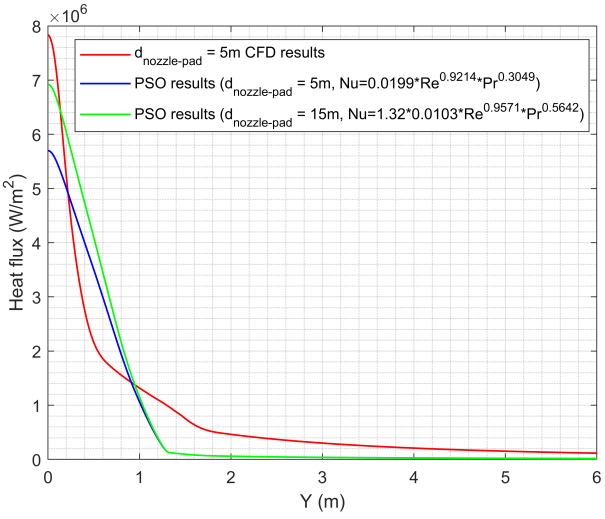

Figure 16. Wall heat flux predicted by CFD results for $d_{nozzle-pad} = 5\ m$, optimized Nusselt correlation for $d_{nozzle-pad} = 5\ m$, correlation obtained with data for $d_{nozzle-pad} = 15\ m$ corrected with calibration constant.

 doi:10.20944/preprints202603.1386.v1

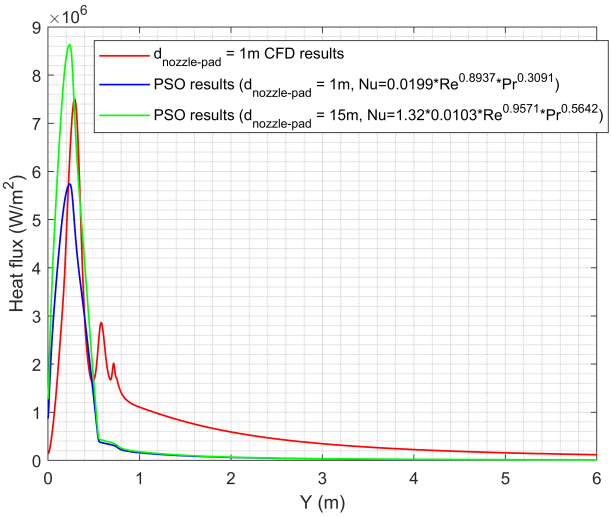

Figure 17. Wall heat flux predicted by CFD results for $d_{nozzle-pad} = 1\ m$, optimized Nusselt correlation for $d_{nozzle-pad} = 1\ m$, correlation obtained with data for $d_{nozzle-pad} = 15\ m$ corrected with calibration constant.

For these reasons, the correlation can be used as a practical preliminary design tool, offering order of magnitude thermal load estimates within seconds compared to the hours or days required for parametric CFD campaigns. However, it must be emphasized that these correlations and their associated error bounds are derived entirely from numerical simulations. Experimental validation under representative conditions (high temperature LOx/CH_4 combustion products, realistic chamber pressures and appropriate standoff distances) is essential before applying these tools to actual landing system design. The CFD results themselves rely on turbulence modeling assumptions ($k-\omega$ SST), frozen flow chemistry and axisymmetric geometry, all of which introduce uncertainties that only physical testing can fully resolve. Future work should prioritize targeted experiments to benchmark both the absolute heat flux predictions and the parametric trends observed in this numerical study.

4. Conclusions

In this work, a comprehensive numerical investigation of supersonic rocket plume impingement during the landing phase of a reusable launcher has been carried out, with specific reference to the Prometheus engine. Axisymmetric RANS simulations were performed to characterize the complex flow field generated by the interaction between the plume and a flat landing surface at different nozzle to pad distances, capturing the effects of shock structures, stagnation regions and turbulence on wall pressure and heat flux distributions.

The results highlighted a strong dependence of surface thermal loads on plume structure and standoff distance. In particular, intermediate nozzle to pad distances were found to produce the highest peak heat fluxes, due to the combined effect of intense velocity and temperature gradients and enhanced turbulent transport. At very short distances, the formation of a stagnation bubble significantly altered the flow topology, redistributing both pressure and heat flux away from the centerline. The study also demonstrated the critical role of spatial discretization accuracy, showing that higher-order numerical schemes are essential to correctly resolve shock–wall interactions and avoid underprediction or misplacement of peak thermal loads.

Based on the CFD database, a simplified engineering correlation for wall heat flux prediction was developed through dimensional analysis and optimized using a Particle Swarm Optimization algorithm. The proposed Nusselt-based correlation, calibrated on a single reference case, proved capable of predicting peak heat fluxes at different standoff distances with acceptable accuracy for preliminary design purposes, generally within conservative error bounds. While the correlation cannot reproduce localized flow features such as stagnation bubbles or secondary maxima, it provides a computationally efficient tool for rapid thermal load estimation during early design phases.

 doi:10.20944/preprints202603.1386.v1

It must be emphasized that all results presented in this study are derived from numerical simulations and are therefore subject to the assumptions inherent in the adopted modeling approach, including turbulence modeling, frozen-flow chemistry and axisymmetric geometry. Consequently, the numerical findings and the proposed correlation should be validated through dedicated experimental campaigns under representative operating conditions before being applied to the design of real landing systems. Such experimental validation represents a crucial step to further increase confidence in the predictive capability of the proposed methodology and to support its extension to more complex configurations.

Funding:

Author Contributions: "Conceptualization, A.R, D.C. and F.B.; methodology, A.R., D.C. and F.P.; software, A.R., D.C. and F.P.; validation, A.R.,D.C. and F.P.; formal analysis, A.R., D.C. and F.P.; investigation, A.R., D.C. and F.P.; data curation, A.R.; writing—original draft preparation, A.R.; writing—review and editing, D.C. and F.B.; visualization, A.R.; supervision, F.B. All authors have read and agreed to the published version of the manuscript.", please turn to the CRediT taxonomy for the term explanation. Authorship must be limited to those who have contributed substantially to the work reported.

Acknowledgments: The authors would like to thank Giovanni Coppola (Italian Aerospace Research Center, Space Propulsion Unit) for his support in the development of the optimized correlations using Particle Swarm Optimization (PSO) and Professor Raffaele Savino (Industrial Engineering Department, University of Naples "Federico II") for supervising the thesis work of Fabio Pisano and for his critical review of the manuscript.

Conflicts of Interest: The authors declare no conflicts of interest.

Abbreviations

The following abbreviations are used in this manuscript:

a	Reynolds number exponential in the Nusselt correlation
b	Prandtl number exponential in the Nusselt correlation
C	Factor in the Nusselt correlation
C_1	Inertia weight factor
C_2	Cognitive attraction weight factor
C_3	Social attraction weight factor
CEA	Chemical Equilibrium Analysis
CFD	Computational fluid-dynamics
$d_{nozzle-pad}$	Distance between the nozzle and the pad, standoff distance
ESA	European Space Agency
GB	Global Best
h_c	Convective heat transfer coefficient
i	Position index
J	Objective function
k	Turbulent kinetic energy
LOx/CH_4	Liquid oxygen/methane
LOx/LH_2	Liquid oxygen/hydrogen
$\dot{m}$	Mass flow rate
N	Number of particles of the swarm
N_{points}	Number of spatial along the impingement surface
Nu	Nusselt number
$Nu_{CFD,i}$	Local Nusselt number from CFD simulation at the $i-th$ position
$Nu_{corr,i}$	Local Nusselt number derived from correlation at the $i-th$ position
O/F	Mixture ratio
p	Iteration index
p_c	Chamber pressure
p_∞	Ambient pressure
PB	Personal Best

 doi:10.20944/preprints202603.1386.v1

Pr	Prandtl number
PSO	Particle Swarm Optimization
q''_{corr}	Heat flux rebuilt with the Nusselt number correlation
RANS	Reynolds Averaged Navier-Stokes equations
Re	Reynolds number
RLV	Reusable Launch Vehicle
SST	Shear Stress Transport
T_0	Total temperature
T_∞	Ambient temperature
T_{wall}	Wall Temperature
TPS	Thermal Protection Sytem
$\underline{V}$	Velocity
VTVL	Vertical Takeoff Vertical Landing
μ_t	Turbulent viscosity
ω	Specific dissipation rate

References

1. SpaceX. *Falcon User's Guide*. SpaceX, 2022. Version 8 - March 2025.
2. Kölle, D.E. *Handbook of cost engineering for Space Transportation systems*; TransCostSystems, 2010.
3. Tománek, R.; Hospodka, J. Reusable launch space systems. *MAD-Magazine of Aviation Development* **2018**, *6*, 10–13.
4. Iannetti, A.; Girard, N.; Tchou-Kien, D.; Bonhomme, C.; Ravier, N.; Edeline, E. Prometheus, a LOX/LCH4 reusable rocket engine. In Proceedings of the Proceedings of the 7th European Conference for Aeronautics and Space Sciences (EUCASS), Milan, Italy, 2017, pp. 1–6.
5. Laureti, M.; Karl, S. Aerothermal databases and load predictions for retro propulsion-assisted launch vehicles (retalt). *CEAS Space Journal* **2022**, *14*, 501–515.
6. Wang, X.; Xu, X.; Yang, Q. Numerical analysis on thermal environment of reusable launch vehicle during supersonic retropropulsion. *International Journal of Thermal Sciences* **2024**, *198*, 108857.
7. Ecker, T.; Karl, S.; Dumont, E.; Stappert, S.; Krause, D. Numerical study on the thermal loads during a supersonic rocket retropropulsion maneuver. *Journal of Spacecraft and Rockets* **2020**, *57*, 131–146.
8. Ecker, T.; Ertl, M.; Klevanski, J.; Krummen, S.; Dumont, E. Aerothermal characterization of the CALLISTO vehicle during descent. *CEAS Space Journal* **2024**, pp. 1–20.
9. Tian, Y.; Li, W.; Xue, P.; Gao, Z. Numerical studies on heat transfer of supersonic combustion-gas jet impingement on perpendicular flat plate. *Heat Transfer Engineering* **2022**, *43*, 864–878.
10. Zuckerman, N.; Lior, N. Jet impingement heat transfer: physics, correlations, and numerical modeling. *Advances in heat transfer* **2006**, *39*, 565–631.
11. Martin, H. Heat and mass transfer between impinging gas jets and solid surfaces. In *Advances in heat transfer*; Elsevier, 1977; Vol. 13, pp. 1–60.
12. Livingood, J.N.; Hrycak, P. Impingement heat transfer from turbulent air jets to flat plates: a literature survey **1973**.
13. Limaye, M.; Vedula, R.; Prabhu, S. Local heat transfer distribution on a flat plate impinged by a compressible round air jet. *International Journal of Thermal Sciences* **2010**, *49*, 2157–2168.
14. Alvi, F.; Ladd, J.; Bower, W. Experimental and computational investigation of supersonic impinging jets. *AIAA journal* **2002**, *40*, 599–609.
15. FR, M. Two-equation eddy-viscosity turbulence models for engineering applications. *AIAA J* **1994**, *32*, 269–289.
16. Wilcox, D.C. Reassessment of the scale-determining equation for advanced turbulence models. *AIAA journal* **1988**, *26*, 1299–1310.
17. Ertl, M.; Ecker, T.; Klevanski, J.; Dumont, E.; Krummen, S. Aerothermal analysis of plume interaction with deployed landing legs of the CALLISTO vehicle. In Proceedings of the 9th European Conference For Aeronautics And Space Science, EUCASS 2022, 2022.
18. Kennedy, J.; Eberhart, R. Particle swarm optimization. In Proceedings of the Proceedings of ICNN'95-international conference on neural networks. ieee, 1995, Vol. 4, pp. 1942–1948.
19. Patel, V.; Rao, R. Design optimization of shell-and-tube heat exchanger using particle swarm optimization technique. *Applied Thermal Engineering* **2010**, *30*, 1417–1425.

 doi:10.20944/preprints202603.1386.v1

20. Peng, H.; Ling, X.; Wu, E. An improved particle swarm algorithm for optimal design of plate-fin heat exchangers. *Industrial & Engineering Chemistry Research* **2010**, *49*, 6144–6149.
21. Zhang, Y.; Wang, S.; Ji, G. A comprehensive survey on particle swarm optimization algorithm and its applications. *Mathematical problems in engineering* **2015**, *2015*, 931256.
22. Babanezhad, M.; Behroyan, I.; Nakhjiri, A.T.; Marjani, A.; Rezakazemi, M.; Heydarinasab, A.; Shirazian, S. Investigation on performance of particle swarm optimization (PSO) algorithm based fuzzy inference system (PSOFIS) in a combination of CFD modeling for prediction of fluid flow. *Scientific Reports* **2021**, *11*, 1505.
23. Coppola, G.; Panelli, M.; Battista, F. Solution of Orifice Hollow Cathode Plasma Model Equations by Means of Particle Swarm Optimization **2024**.
24. Sutton, G.P.; Biblarz, O. *Rocket propulsion elements*; John Wiley & Sons, 2011.
25. Huzel, D.K. *Modern engineering for design of liquid-propellant rocket engines*; Vol. 147, AiAA, 1992.
26. https://www.esa.int/ESA_Multimedia/Images/2017/06/Prometheus.
27. Menter, F.R. Two-equation eddy-viscosity turbulence models for engineering applications. *AIAA journal* **1994**, *32*, 1598–1605.
28. Menter, F.R.; Kuntz, M.; Langtry, R.; et al. Ten years of industrial experience with the SST turbulence model. *Turbulence, heat and mass transfer* **2003**, *4*, 625–632.
29. Wilcox, D.C.; et al. *Turbulence modeling for CFD*; Vol. 2, DCW industries La Canada, CA, 1998.
30. Menter, F.; Ferreira, C.; Esch, T.; Konno, B. The SST Turbulence Model with Improved Wall Treatment for Heat Transfer Predictions in Gas Turbines,'International Gas Turbine Congress 2003, Tokyo. Technical report, IGTC2003-TS-059, 2003.
31. https://webbook.nist.gov/.
32. Edeling, W.N.; Schmelzer, M.; Dwight, R.P.; Cinnella, P. Bayesian predictions of Reynolds-averaged Navier–Stokes uncertainties using maximum a posteriori estimates. *AIAA Journal* **2018**, *56*, 2018–2029.
33. McConkey, R.; Kalia, N.; Yee, E.; Lien, F.S. Turbo-RANS: straightforward and efficient Bayesian optimization of turbulence model coefficients. *International Journal of Numerical Methods for Heat & Fluid Flow* **2024**, *34*, 2986–3016.